Thermal Interaction of Inert Additives in Energetic Materials

by

Gwendolyn Tsai

Submitted to the Department of Mechanical Engineering
in partial fulfillment of the requirements for the degree of

MASTER OF SCIENCE IN MECHANICAL ENGINEERING

at the

MASSACHUSETTS INSTITUTE OF TECHNOLOGY

May 2024

Authored by: Gwendolyn Tsai
Mechanical Engineering
May 9, 2024

Certified by: Sili Deng
Assistant Professor of Mechanical Engineering, Thesis Supervisor

Accepted by: Nicolas Hadjiconstantinou
Professor of Mechanical Engineering
Graduate Officer

Thermal Interaction of Inert Additives in Energetic Materials

by

Gwendolyn Tsai

Submitted to the Department of Mechanical Engineering
on May 9, 2024 in partial fulfillment of the requirements for the degree of

MASTER OF SCIENCE IN MECHANICAL ENGINEERING

ABSTRACT

Energetic materials are used for a variety of applications, including airbag deployment and solid rocket fuels, that require high energy density and various energy release rates. The energy release rate, determined by how fast the material burns, is often thought to be proportional to the bulk thermal diffusivity of the material. However, the inclusion of insulating inert particles in energetic materials has shown burning rate enhancement in certain cases. Flame front corrugation that increases the reaction front area observed at micron to sub-millimeter scales was proposed previously to explain the phenomenon. However, a recent simulation study observed a significant temperature gradient within the inert particle, implying that the residence time of the inert particle in the flame front could play a role in the thermal interaction between additives and surrounding energetic materials. In this work, we tested these hypotheses by employing a high-speed microscopic imaging system to quantify the burning rate and flame morphology of Al/CuO nanothermites with various SiO_2 particle sizes and mass loading. Additionally, we performed flame propagation simulations to quantify the thermal interactions between the energetic materials and the embedded single inert particle. The experimental results show that the burning rate depends on the particle size as well as mass loading. Specifically, as the SiO_2 particle size increases from 100 nm to 100 μm, the burning rate is enhanced by 26% at a mass loading of 7.5%. Further computational studies reveal that flame corrugation may not be the sole factor to alter the burning rate. Non-dimensional analyses show that energy absorption and temperature non-uniformity in inert particles have strong correlations with particle diameter. When the characteristic time of heating the inert particle is shorter than the flame residence time, the inert particle acts as a heat sink, leading to a negative impact on burning rates due to the heat removal from the surrounding energetic materials. Experimental studies reveal that additive particle size has an impact on the nanothermite burn rate. Insight into why this may occur is provided by computational studies of a single particle inclusion, as well as images captured of the burn rate experiments, showing the flame front morphology and particle size effects on heat transfer may play a key role in burn rate alteration by inert additives.

Thesis supervisor: Sili Deng
Title: Assistant Professor of Mechanical Engineering

Acknowledgments

I would like to thank my advisor, Professor Sili Deng, for her support throughout the conception and execution of this project. I would also like to thank her for her support in the development of my own goals and interests as both a researcher and an engineer. I would like to thank Dr. Suyong Kim for his close guidance on this project, as well as his constant positivity and encouragement throughout my time in graduate school. I would also like to express my appreciation for the entire DENG energy and nanotechnology group including Maanasa Bhat, Stefan Borjan, Huaibo Chen, Zituo Chen, Benjamin Koenig, Dr. Qiaofeng Li, Emily Lin, Edoardo Ramalli, Nick Tricard, Dr. Linzheng Wang, Chuwei Zhang, and Dr. Jianan Zhang. I feel very lucky to have worked in such a collaborative and supportive group where I have learned so much from my lab mates.

I would like to express my gratitude to the SMA SOE Fellowship and the NASA Space Technology Graduate Research Opportunity (grant no. 80NSSC23K1222) for supporting my research. I also appreciate the help of George Story, our collaborator at NASA Marshall. I would also like to thank Jim Bales and the Edgerton Center for the help I have received with the high-speed photography that was instrumental to this work. I would also like to acknowledge MIT Nano and the MIT Material Research Laboratory for providing training and access to the scanning electron microscopes used in this work.

I'd like to thank my friends at MIT for making lunches, problem sets, coffee breaks, and life in general at MIT fun. I am so grateful for all the support I have received through this journey and I am constantly inspired by those around me.

Finally, I would like to thank my family. I would like to thank my mom for her unwavering support of my academic career, and for always being a phone call away for advice or a simple pep talk. I would like to thank my dad for constantly reminding me to enjoy the work I do and appreciate the world around me. I would also like to thank my sister, Anna, and my boyfriend, Jak, for being there for me during the ups and downs of graduate school.

Contents

List of Figures

List of Tables

Chapter 1

Introduction

1.1 General Approaches to Burn Rate Tunability

Nanothermites are composed of nano-sized metal/metal oxide composites that can undergo redox reactions. They are studied as systems of interest due to their high energy density and reactivity for energetic applications [1]. They also represent a relatively simple chemistry model system for fundamental studies of solid combustion of energetic materials. Novel applications of nanoenergetics have demonstrated the capability for rapid circuitry actuation, soft robotics, and biomedical microfluidics, making remote operation of medical devices possible [2–4]. However, the most common use cases for nanothermites and other nanoenergetic materials are satellite and rocket propellants.

Some of the advantages of solid rockets include their simplicity (lack of moving parts), storage stability, rapid deployment capability, and high volumetric impulse when compared to liquid and hybrid rocket engines. This makes them attractive for defense and volume-limited applications. The main limitation of solid rockets is that they are not throttleable, once a fuel grain is cast the trust profile is set. Additionally, casting can only create a limited number of geometries due to practical manufacturing constraints. The thrust profile is determined by fuel grain shape and composition. The composition of the fuel determines the regression or burning rate. This is often modeled empirically by St. Robert's law (Eq. 1.1) which relates burning rate (r_b) to combustion chamber pressure (p_c) using a burning rate coefficient (a) and a burning rate exponent (n) to fit experimental data [5].

$$r_b = ap_c^n \tag{1.1}$$

One prominent effort to overcome these limitations is the development of "smart energetics" or materials whose burning rate can be modulated using external stimuli. One approach to developing active control methods exploits the piezoelectric effect observed in some polymers and high-explosive crystals. The work of Janesheski et al. has demonstrated that the application of a direct current voltage on nano aluminum/ piezoelectric polymer composites changes the sensitivity of the composite, allowing for lower impact energy ignition in drop tests [6]. Possible mechanisms that have been proposed for this observed change in ignition properties are induced mechanical deformation and dielectric breakdown, both as potential causes of hotspot formation [7]. A similar phenomenon has also been observed in other Hydroxyl ammonium nitrate-based solid propellants as their ignition delay time and burn rate can both be modulated through the application of an electric field [8]. This is just one method, others include the application of microwaves [9] and lasers [10]. Outside of their low technology readiness level, there are other significant technical challenges associated with this technology, most prominently the addition of high-energy complex systems for burn rate modulation.

An alternate approach to achieving a desired thrust profile is through varying both fuel geometry and composition. This has been previously implemented with cast fuel grain shapes such as the "wagon wheel". Casting, the legacy method of manufacturing solid fuel grains, can only achieve relatively simple geometries. However, additive manufacturing is a promising candidate for fuel grain construction. Recent work has demonstrated the ability to manufacture propellants with complex geometries [11] and high solids loading [12, 13], achieving comparable performance to cast grains and the ability to modulate burn rate through control of printing infill density. Additive manufacturing also provides the option to use multiple fuels and oxidizers in a single grain, allowing additional degrees of freedom during the development of the motor's thrust profile by modulating the propellant burn rate in different locations in the fuel grain.

1.2 Fuel Additives

Additives are a common way to improve performance and alter the burning rate of solid fuels and energetic materials. Developed high-performance novel energetics have largely not been put into use due to high cost and thermal instability issues, leaving the use of additives as the most efficient way to improve the performance of energetic compounds [14]. Additive approaches include the utilization of catalysts, embedded reactive wires, and the use of an energetic binder [15]. These are guided by the physical intuition that increasing the energy density or the speed of reaction chemistry will result in a faster burning rate and therefore higher performance.

For the same reason, inert additives seem to be a logical candidate for reducing the burning rate. According to the classical combustion theory on laminar flame speed, the flame speed r_b is proportional to both the thermal diffusivity α and the chemical reaction rate $\dot{\omega}$, such that $r_b \propto \sqrt{\alpha\dot{\omega}}$. Therefore, insulating inert additives that result in a lower overall reactivity and have low thermal transport properties are expected to result in a reduced burning rate. However, some experimental work has found the opposite.

Wang et al. studied the burning rate behaviors of Al/polyvinylidene fluoride (PVDF) films created by electrospray deposition, a somewhat novel manufacturing method used to achieve high mass loading of aluminum in mechanically flexible films [16]. Mesoporous SiO_2 with a diameter of 0.2–4 μm was used as an additive. The addition of 5 weight percent SiO_2 resulted in a burning rate three times faster than the baseline [17]. Kline et al. found that the addition of insulating 1–5 μm SiO_2 particles to Al and PVDF 3D printed films resulted in an increase in the burning rate from ∼15 cm/s to ∼23 cm/s. Furthermore, the addition of conductive graphite flakes decreased the burning rate to ∼6 cm/s [18]. Julien et al. also observed a similar result contradictory to laminar flame theory when adding insulating inert particles to alternating Al (75 nm thick) and CuO (150 nm thick) nanolaminates. The addition of thermally insulating SiO_2 with a particle size of 150 nm increased the burning rate by 30%. However, the addition of thermally conductive gold with a particle size of 5-30 nm also resulted in an increase in the burning rate of 117% [19].

This presents an interesting problem, as the addition of inert insulating SiO_2 has increased

the burning rate across multiple film compositions and synthesis methods, contrary to what laminar flame theory would suggest. The addition of thermally conducting particles has also had conflicting observations, as a result, no consensus has been reached on these burning rate alterations with inert particles. To understand the physical mechanisms of how thermally insulating and conductive particle inclusion can alter the burning rates, Kline et al. measured the flame morphology at a resolution of $\sim$1 μm/pixel. They found that thermally insulating particles plausibly led to the flame front corrugation on a 100 μm scale, increasing the surface area of the flame front and potentially providing an explanation for the increased burning rate [18]. Julien et al. also further analyzed the burning morphology of an Al/CuO nanolaminate system with both experimental and simulation studies [19]. The analysis showed that larger thermal gradients around and in an inert particle could potentially contribute to the increased burning rate.

The previous efforts to elucidate the burning rate alteration mechanisms have consistently argued that flame front corrugation can dominantly determine the burning rate. However, since a significant temperature gradient in the inert particle was observed in the work of Julien et al. [19], we further hypothesize that thermal interaction between an inert particle and surrounding energetic materials could additionally change the reaction rates near the inert particles. However, these heat transfer effects by inert particles highly depend on the particle size and the flame residence time passing through the inert particles, which can result in inconsistent burning rate alteration with conductive and insulating inert particles.

1.3 Scaling Effects

Interest in nanoenergetic materials has stemmed from the favorable properties of nanoparticles including smaller diffusion length scales and heat capacity, in addition to higher surface area to volume ratios, which are favorable for rapid heat transfer into the particle [1]. This interest was bolstered by the experimental observations of significantly higher burning rates when aluminum nanoparticles were added into propellant mixtures compared to micron-sized particles [20, 21]. The dependence of particle burning time (t_b) on diameter is often described by a d^n law. The expected value for n in the d^n law comes from an analytical solution for

particle combustion. This solution is developed for two cases: diffusion-limited reactions, modeled similarly to droplet combustion, and kinetics-limited reactions, approximated as a metal burning in a pure oxygen environment with surface reactions. The traditional "shrinking particle" theory expects that Micron-sized particles exhibit diffusion-controlled combustion (Eq. 1.2), while nano-sized particles are expected to be kinetically limited (Eq. 1.3). [1, 22].

$$t_{b,diff} \sim d_0^2 \tag{1.2}$$

$$t_{b,kin} \sim d_0 \tag{1.3}$$

For micron-sized and larger particles, experimental values for n are most often between 1.5 and 2 [23]. This provides a reasonable level of agreement with the theory. This trend however does not hold at a nanometer scale, where n has been observed to be around 0.3. Traditional kinetically limited combustion theory predicts a n value of 1, suggesting that complex factors such as particle agglomeration and condensed phase reactions become important in the burning behavior of nano-sized particles [23]. This is also consistent with experimental observations completed in heterogeneous shock tubes that show there are higher concentrations of Al vapor present in reactions with micron-aluminum than reactions with nano-aluminum [24].

In the condensed phase, nanoparticle sintering (also referred to as aggregation) has been observed. This occurs when particles are rapidly heated and can counter-diffuse and react without entering the vapor phase. This often occurs early in the reaction, changing the starting length scale (d_0) of the particle [25]. More complex models have also suggested that at the nanometer scale induced electric fields and mechanical stress on the oxide shell can also contribute to the reaction mechanisms [26].

It is clear that for reacting particles scaling effects play an important role in determining the microscopically observed burning rate and the mechanisms of how the reaction progresses. Scaling effects in additives, however, are not as well documented or understood. As previously discussed, flame speed is thought to increase with the addition SiO_2 due to

the formation of hot spots and the induction of flame front corrugation. It has also been suggested through DSC analysis that catalytic interactions between SiO_2 and Al/PVDF may play a role in the burn rate acceleration [17]. By investigating scaling effects in additives we hope to better understand the mechanisms for flame front alteration and the importance of the additive size in its interaction with the fuel, oxidizer, and binder.

1.4 Experimental Approaches for Understanding Nanothermite Combustion

One of the most common metrics used to quantify the performance of an energetic material is the linear burn rate. Measurement of the linear burn rate is completed by using high-speed photography to track the movement of the flame front over time. More advanced setups utilize microscopic imaging and color camera pyrometry to assess flame front morphology and temperature distribution with micron-scale resolution With these added features, experiments are capable of measuring linear burn rate, in addition to observing microscopic behavior that can be used to comment on physical mechanisms determining the burning rate. For example, the formation of hot and cold spots that are about the size of micron fuel additives has been observed in experiments with high-resolution pyrometry [18, 19]. Additionally, microscopic imaging of local flame front propagation has been used alongside pyrometry to evaluate the particle sintering time scale. This time scale was determined to be significantly faster than the time scale for heat transfer between the reacted particles and the fuel/environment, making this cooling time scale the rate-limiting step for the reaction [27]. From these observations, it is clear that microscopic high-speed imaging provides significant advantages for the observation of reaction mechanisms compared to macroscopic imaging of the burning rate.

Beyond mechanical mechanisms determining reaction speed, there is also an interest in measuring the kinetics of any given fuel, oxidizer, and binder mixture. The most conventional methods for measuring condensed-phase reaction kinetics are differential scanning calorimetry (DSC) and thermogravimetric analysis (TGA). DSC and TGA measure heat release and

mass change of a sample respectively as it is heated slowly, generally on the order of 10°C per minute. Data from DSC and TGA can be used for determining phase change temperatures, reaction enthalpies, and catalytic effects [17] [28]. The main limitation of TGA and DSC is the low heating rates. The mechanisms observed at these heating rates may differ from those that are relevant during the high heating rates in combustion. However, there have been efforts to overcome this limitation. A method utilizing mass spectrometry has achieved time-resolved characterization of decomposition at heating rates as high as 10^5 °C per second [29].

Finally, these observations are often supplemented with analysis of product and reactant morphology using high-resolution tools capable of viewing a single nanoparticle. To achieve imaging at a resolution this high, a scanning electron microscope (SEM) or transmission electron microscope (TEM) is often used. Visual analysis of combustion products has aided in understanding the role of sintering in nanomaterial combustion. Nanometer-resolution imaging is useful for this application because sintering results in the formation of aggregates of nanoparticles, dramatically changing the product morphology [25].

1.5 Research Objectives

The goal of the study is to understand the heat transfer mechanisms between active energetic materials and inert particles. It is clear that the addition of insulating SiO_2 results in an increase in burning rate across multiple types of energetic systems, including nanolaminates and nanothermite films. This increase in the burning rate is contradictory to laminar flame theory and can not be explained by the bulk properties of the film. Additionally, energetic particle size effects have a well-documented influence on the burning rate. Considering both of these factors, we have developed a hypothesis that particle size effects may play a role in this unexplained increase in burn rate through thermal interaction between the particle and the flame. The extent of the interaction between the particles is determined by the residence time of the flame, which is determined by both particle diameter and flame front distortion/corrugation. To test our hypotheses regarding the influences of particle size and flame residence time, we investigated the burning rate alteration by varying the size of SiO_2

inert particles to modulate the residence time and flame morphology, and the mass loading to understand the coupling of heat transfer and flame corrugation in Al/CuO nanothermite films. We first quantified the influence of inert particle diameter and mass loading on the burning rate via high-speed microscopic imaging of the reaction front. Then, computational studies examined thermal interactions at the particle scale, simulating a single inert particle embedded in energetic composites. Finally, we discussed the non-dimensional analysis to elucidate the roles of heat transfer interaction between energetic composites and inert particles on the burning rates with three metrics, including flame front corrugation, heat loss in energetic materials, and temperature non-uniformity in an inert particle. By developing a systematic understanding of the impact of inert additives on energetic performance, the design of energetic materials will be more accessible for tunable performances.

Chapter 2

Experimental Methods

2.1 Precursor Solution Preparation

Nanothermite powder and precursor solution with inert additives were prepared by a physical mixing process, as described in [27, 30]. First, a binder solution was prepared by mixing 62.5 mg of polyvinylidene fluoride (PVDF) and hydroxypropyl methylcellulose (HPMC) in 4 ml of dimethylformamide (DMF) using a magnetic stirrer for 4 hours, until the solution was homogeneous and transparent. Then, a total amount of 1125 mg of aluminum (Al, 100 nm in diameter, US Research Nanomaterials, Inc.), copper oxide (CuO, <50 nm in diameter, Sigma-Aldrich), and silicon dioxide (SiO_2, see below for the details) particles were added to the binder solution. Therefore, the total particle loading was set to be 90%, and masses for Al, CuO, and SiO_2 were calculated based on the loading of SiO_2. The binder solution was mixed with powders in a high-speed mixer at 800 rpm for 10 minutes. Finally, the precursor solution was transferred to the syringe for film fabrication.

In all cases, the equivalence ratio was fixed at three, based on the active content of Al. For example, 454.5 mg of Al and 670.4 mg of CuO were included in a baseline solution without SiO_2. The diameters of the SiO_2 were varied from 10 nm (smaller than the size of Al and CuO) to 25 μm (larger than the size of Al and CuO). We purchased SiO_2 from Sigma-Aldrich (10-20 nm, 0.5-10 μm), and from US Research Nanomaterials, Inc. (60-70 nm, 200 nm, and 25 μm).

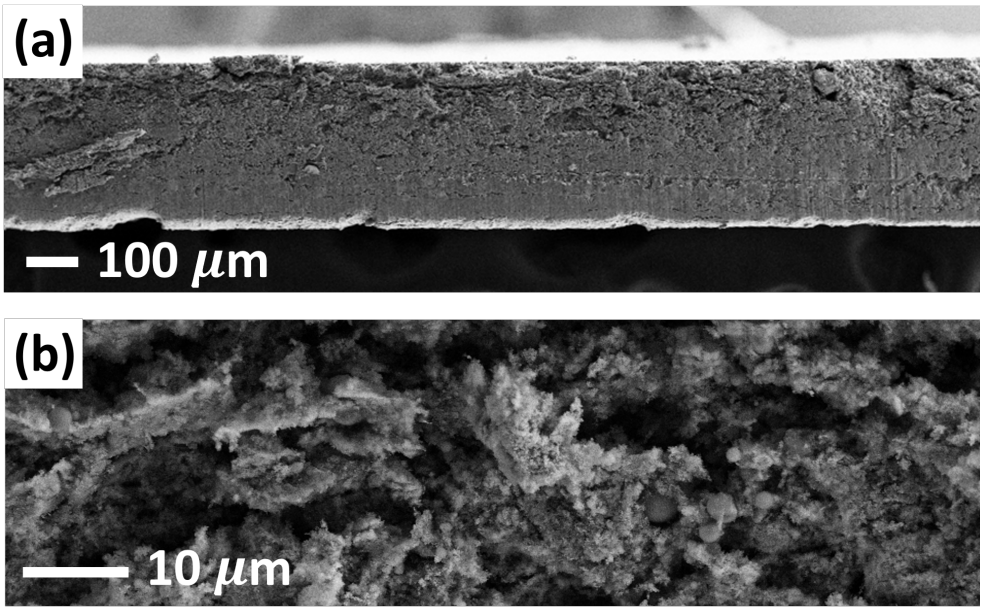

Figure 2.1: Scanning electron microscopy images of the Al/CuO nanothermite film cross-section (a) under 500× magnification and (b) 10k× magnification.

2.2 Film Fabrication

Nanothermite films were created using a coating applicator with a 400 μm standoff height on glass microscope slides [30]. First, a microscope glass was masked using a polyester tape, providing a uniform width of 3 mm. Then, the glass slide was placed on a hot plate heated to 85°C, where it remained for the entirety of the fabrication process. After a drop of precursor solution was loaded on one end of the glass, a coating applicator was slid over the glass to form a thin liquid film to be dried. This coating process was repeated until the film thickness reached ∼350 μm (Fig. 2.1). The nanothermite film was peeled off from the glass substrate and transferred to the imaging setup.

2.3 High-Speed Microscopic Imaging

To characterize flame morphologies and quantify burning rates at sub-millimeter scales, a high-speed microscopic imaging system was used, shown in Fig. 2.2 [30]. One end of the prepared nanothermite film was fixed as a cantilever structure above a 5× microscope

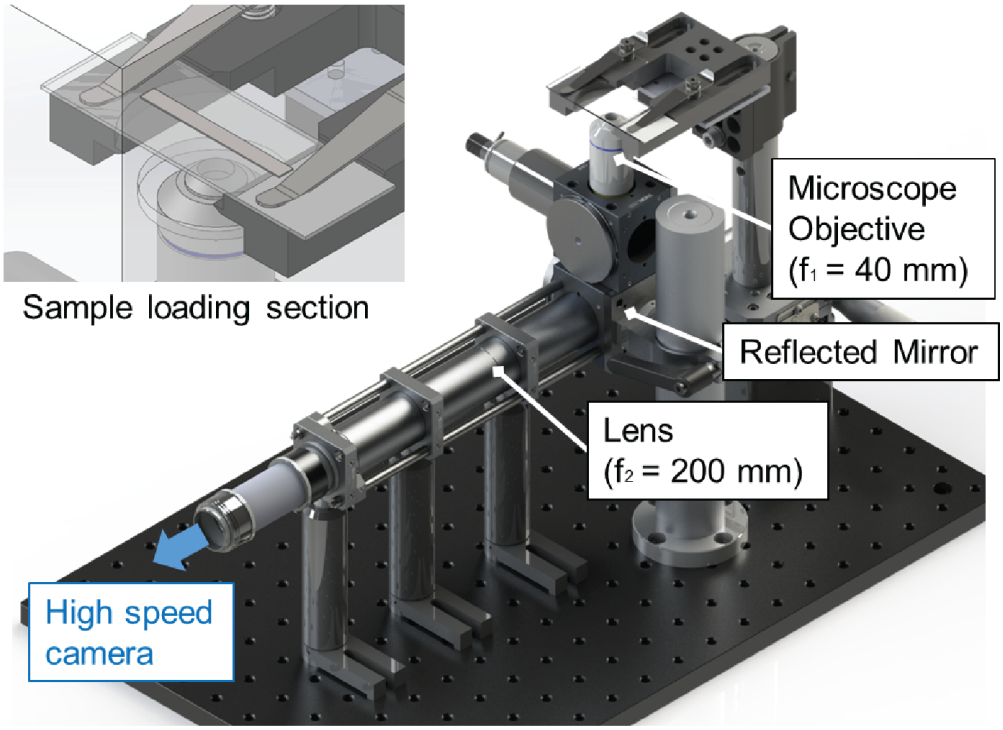

Figure 2.2: High-speed imaging system used to measure burn rate of nanothermite films, developed in Kim *et al.* [30]

objective in the test section. Then, the other end was ignited by a hot wire. The images were captured by a high-speed video camera (Photron AX200) at 20,000 fps with an exposure time of 1/25,000 seconds. The imaging quality was 640 x 480 pixels and captured a window that was approximately 2.2 mm x 1.7 mm, resulting in a resolution of 3.58 μm/pixel.

2.4 Collection of Combustion Products

To understand the role additives may have in altering reaction mechanisms, such as particle sintering, combustion products were collected and analyzed. During burn rate tests, a glass microscope cover slip was placed over the front lens of the microscope objective. This protected the objective from damage, as hot products would often be ejected from the film in all directions, including toward the objective. These glass coverslips were collected for a baseline case, 2.5 wt% 10-20 nm SiO_2 and 0.5-10 μ SiO_2. Products on the glass coverslips were then brought to the SEM for observation of product size and morphology.

2.5 Flame Speed Calculation

To quantify the burning rates, high-speed images were captured and processed to find the flame front location over time using binarization edge detection. This process is depicted in Fig. 2.3 and can be described in four steps.

a. High-speed images of the flame are captured using the experimental setup described above.

b. Images are converted into black and white.

c. Images are binarized using cv2, a python module for image processing. The threshold value is set to 64 (out of 255)

d. The leftmost pixel above the binarization threshold is determined to be the location of the flame front in every row. This is based on a flame propagation direction from right to left.

e. Pixel size calibration and frame rate are used to calculate the flame speed (not shown).

At times, this method can be prone to noise. Two common sources of noise were sparks coming off the flame front, and dark spots along the flame front that appeared as gaps. Both of these issues are depicted in Fig. 2.4.

A moving average filter was used to filter out noise in the flame front prediction data caused by these issues. To implement this filter, a forward and backward exponentially weighted mean was calculated around a point with a span of 125. The average value of the forward and backward mean was then taken. If measured values had a deviation of greater than 50 pixels from that average it was removed from the data set. In some cases, the combustion products fell on the microscope objective, or there was additional noise associated with the beginning and end of a data collection round, so the data was also trimmed to ensure only regions of even burning were used in the calculation. The results of filtering and trimming the raw predictions of flame front location for the sample show in Fig. 2.4 are shown in Fig. 2.5.

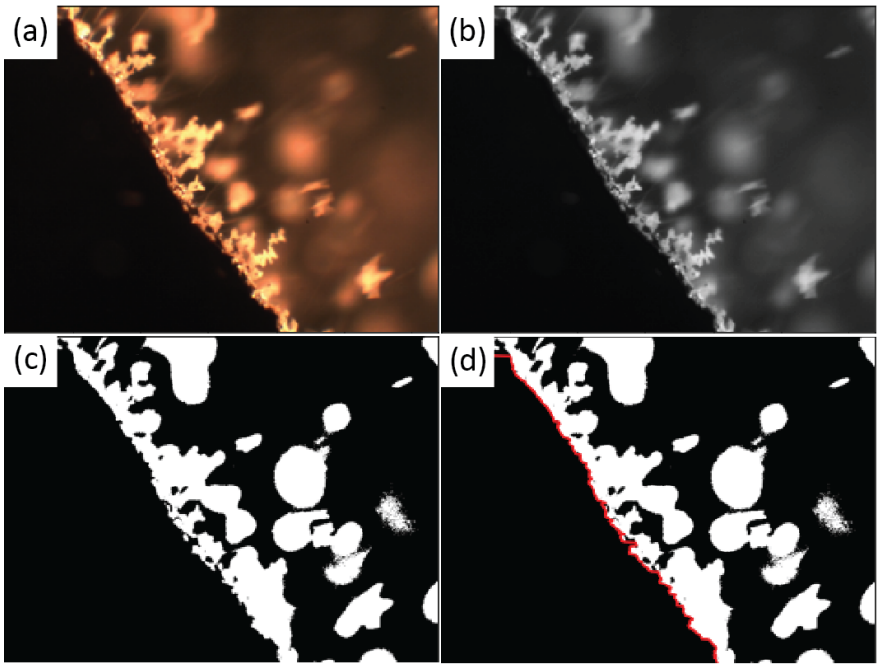

Figure 2.3: Binrization method of flame front detection shown on 2.5 wt% 10-20 nm SiO sample. (a) capture image is converted to (b) black and white and then (c) binarized, where the (d) left most location of light is determined to be the location flame front, displayed in red.

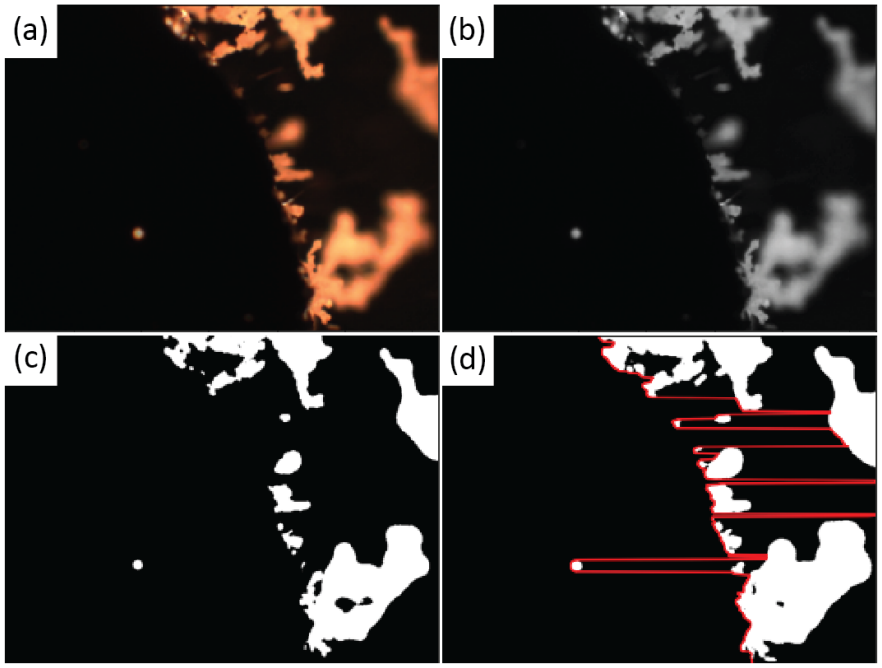

Figure 2.4: Issues in binarization flame front detection arising from dark spots and sparks. Shown on a control sample.

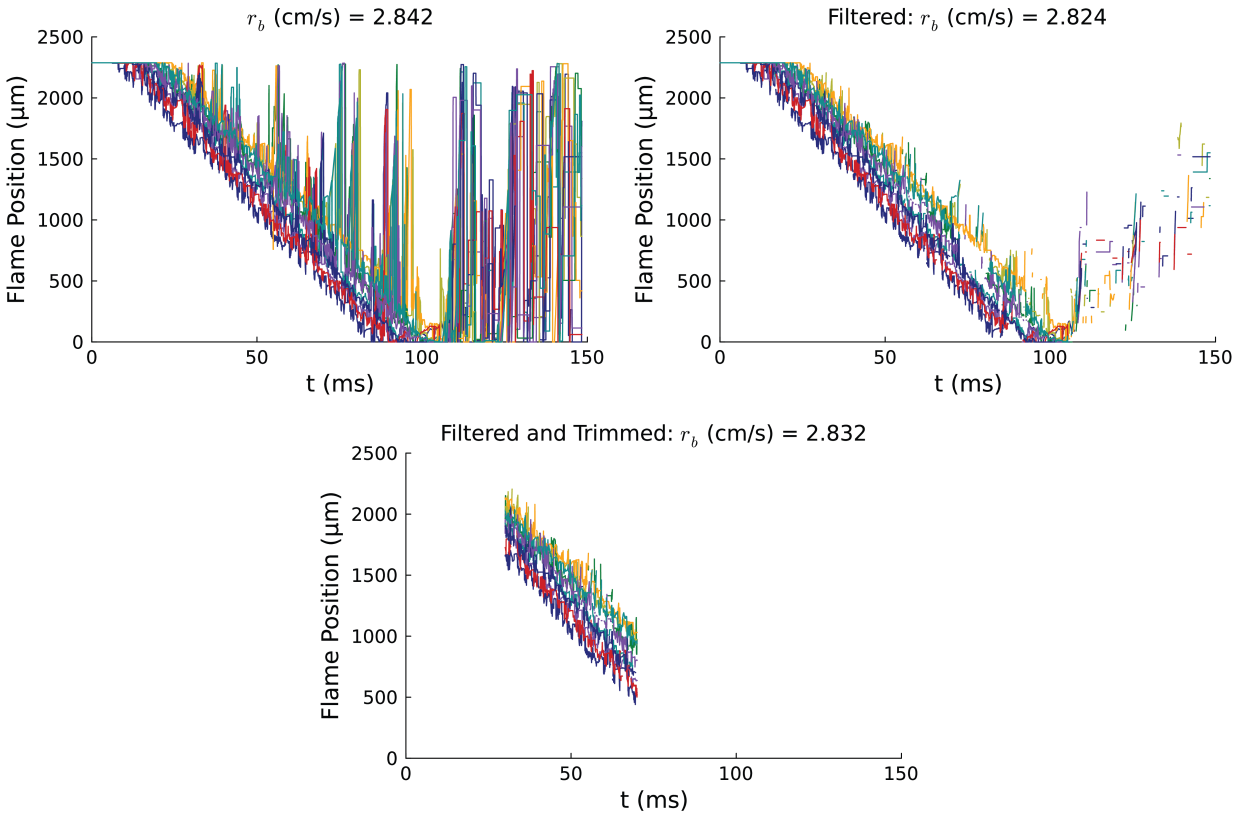

Figure 2.5: Flame front location at ten locations over time. Raw data, filtered data, and filtered/ trimmed data are shown.

Chapter 3

Simulation Methods

3.1 Overview

To understand the heat transfer mechanisms with inert particle additives, we developed a computational model that accounts for thermal structures in and surrounding an inert particle. A transient heat equation was adopted to simulate the flame propagation, given state variables of temperature $T(x, y, t)$ and progress variable $\omega(x, y, t)$, where x and y are the spatial coordinates and t is the time. The Arrhenius rate equation and a one-step global reaction were implemented, as in [31], with an assumption of a complete reaction.

$$\rho C_p \frac{\partial T}{\partial t} = \nabla \cdot (k \nabla T) + H_r \frac{\partial \omega}{\partial t}, \tag{3.1}$$

$$\frac{\partial \omega}{\partial t} = A(1-\omega)\exp(-\frac{E_a}{RT}), \tag{3.2}$$

where ρ is the density, C_p is the heat capacity, k is the thermal conductivity, $H_r = C_p(T_f - T_0)$ is the heat of reaction, A is the pre-exponential factor, E_a is the activation energy, and R is the universal gas constant.

To account for the different particle sizes and to apply the consistent mesh density to all simulation cases, Eqs. (3.1-3.2) were non-dimensionalized such that

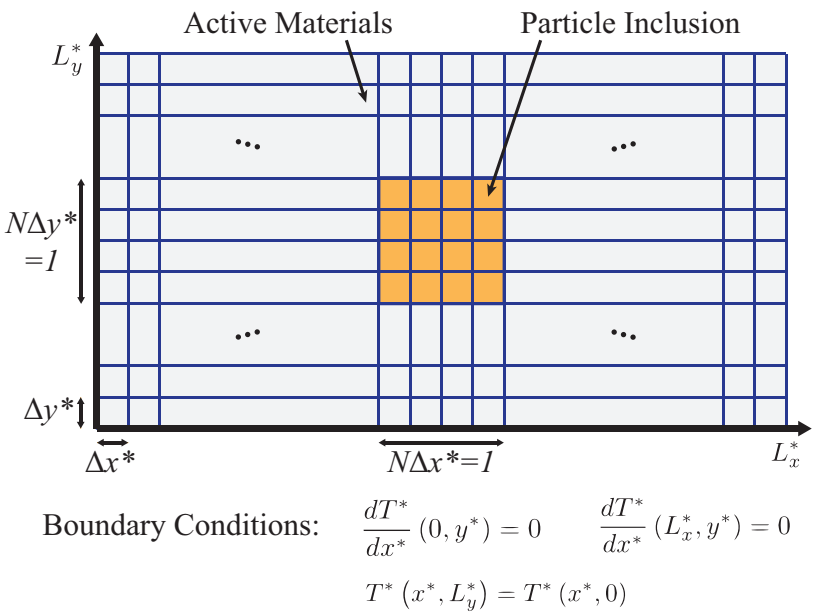

Figure 3.1: Non-dimensionalized simulation domain and boundary conditions. Grey and orange shaded areas indicate the active materials and the inert particle, respectively. Neumann boundary conditions were adopted at x^*=0 and L_x^*. Periodic boundary conditions were adopted at y^*=0 and L_y^*.

Table 3.1: Material properties and kinetic parameters used in the simulation. Active materials are the composite of Al/CuO/PVDF/HPMC, and the inert particle is SiO_2.

Description	Value	Unit	Reference
ρC_p	3.52	MJ/m^3-K	[32]
k_{active}	3.5	W/m-K	[31]
k_{SiO_2}	1.1	W/m-K	[32]
T_f	2844	K	[31, 33]
A	1.41×10^5	s^{-1}	[34]
E_a	80	kJ/mol	[34]
R	8.314	J/mol-K	[32]

$$T^* = \frac{T - T_0}{T_f - T_0}, \quad \omega^* = \omega, \tag{3.3}$$

$$x^* = \frac{x}{D}, \quad , y^* = \frac{y}{D}, \quad t^* = \frac{r_b}{D}t, \tag{3.4}$$

where the superscript * refers to the non-dimensional parameters, T_0 is the ambient temperature, D is the inert particle diameter, and r_b is the burning rate. The value used for the burning rate is obtained from the baseline with no additives in experiments.

The simulation domain is illustrated in Fig. 3.1. The mask is placed at the center of

the domain, representing a single inert particle embedded in active materials. Since the thermal conductivity varies in space, a subgrid was implemented to compute the thermal conductivity at the interface of an inert particle and its surrounding [35] such that

$$k_{i+\frac{1}{2},j} = \frac{2k_{i,j}k_{i+1,j}}{k_{i,j} + k_{i+1,j}}. \tag{3.5}$$

Furthermore, in an inert particle, the reaction rate was forced to zero. The mesh was created to section an inert particle by $N > 40$. Therefore, the mesh size was given by $\Delta x^* = \Delta y^* = 1/N$. The Neumann boundary conditions were adopted at $x^* = 0$ and L_x^*, and the periodic boundary conditions were adopted at $y^* = 0$ and L_y^*. Due to the periodic boundary condition, the domain size along the y direction reflects the distance between two inert particles. The discretized state variables of $T(x, y, t)$ and $\omega(x, y, t)$ were vectorized, and solved using an ordinary differential equation solver of an explicit Tsitouras 5/4 Runge-Kutta method.

This simplified model was intended to comprehend thermal interaction between flame fronts and an inert particle, similarly in [35]. Therefore, it does not consider more complex phenomena such as flame heterogeneity by reactive sintering and porous structures and multi-step chemical reactions. Due to these limitations, the computational works completed focus on micron-sized particles, with particle diameters ranging from 10 to 1,000 μm.

The material properties and the kinetic parameters used in this paper can be found in Table 3.1. Density was calculated by taking reference values for aluminum and copper oxide [32] and using a weighted average based on mass percentage at an equivalence ratio of $\phi = 3.0$. Adiabatic flame temperature was calculated using thermal properties of aluminum, aluminum oxide, and copper (See Section 3.2). Due to the lack of available kinetic data, A and E_a were tuned iteratively to achieve the experimentally observed burning rate and a flame thickness, within the bounds of the values given by differential scanning calorimetry (DSC) in Umbrajkar et al. [34]. In addition, the thermal conductivity of active materials (Al/CuO/PVDF/HPMC) was also calibrated in the same regard, within the bounds of the values in Epps et al. [31].

3.2 Calculation of Adiabatic Flame Temperature

Adiabatic flame temperature of the Al/ CuO nanothermite was calculated using Eq. 3.6 where H_{rxn} is the enthalpy of the reaction, C_p is heat capacity, T is temperature, and $\Delta H_{phase\ change}$ is the enthalpy associated with any relevant phase transitions occurring in the temperature interval evaluated.

$$\Delta H_{rxn} = \int_{T_0}^{T_f} C_p(T)\, dT + \Delta H_{phase\ change} \tag{3.6}$$

Heat capacity was modeled using the Shomate Equation (Eq. 3.8). The Shomate constants $(A - E)$ and the melting/ boiling temperatures, were from the NIST Chemistry WebBook [32].

$$C_p = A + Bt + Ct^2 + Dt^3 + E/t^2 \tag{3.7}$$

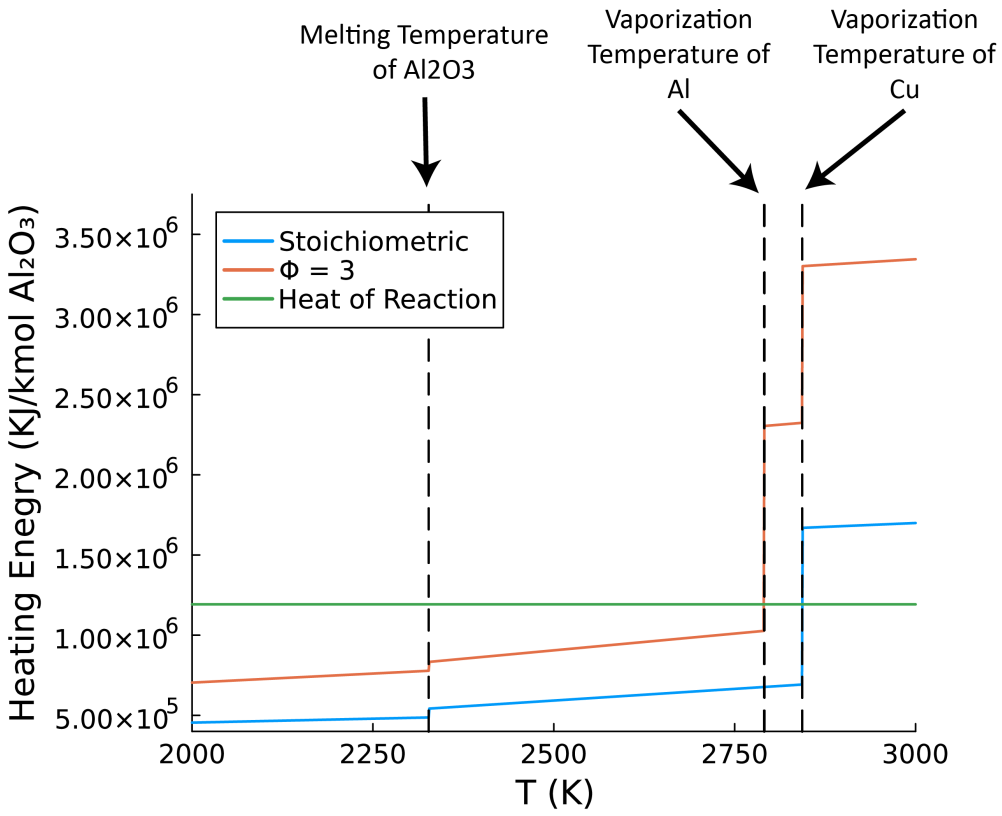

Figure 3.2: Calculated heating energy associated with product temperature for equivalence ratios of one and three

The latent heat of melting and vaporization were calculated using the enthalpies of formation for solid, liquid, and gaseous Al_2O_3, Cu, and Al when relevant. The composition of reactants and products was determined using the sociometric equation shown below where ϕ is the equivalence ratio.

$$3CuO + 2\phi Al \longrightarrow 3Cu + Al_2O3 + (2\phi - 2)Al \tag{3.8}$$

To ensure the accuracy of this calculation, the adiabatic flame temperature was first computed for an equivalence ratio of one. This result was consistent with the value in literature, 2843 K (the vaporization temperature of Cu) [33]. The adiabatic flame temperature used in simulation works was 2789 K, the result for an equivalence ratio of three.

The adiabatic flame temperature for an equivalence ratio of three occurs at the vaporization temperature (boiling point) of aluminum. At an equivalence ratio of one, there is no aluminum present in the combustion products, so the adiabatic flame temperature occurs at the vaporization temperature of copper. With the addition of SiO_2, as completed experimentally, the adiabatic flame temperature would be further reduced below both of these vaporization temperatures, resulting in additional non-gaseous products.

3.3 Mesh Convergence

A mesh convergence test was completed by simulating the flame propagation over a single particle with a diameter of 100 μm and a domain height of 1,000 μm. Based on the result presented in Figures 3.3 and 3.4 a value of 50 was selected for N, meaning the mesh size on

Table 3.2: Corresponding N value (used for nondimensionalization) and element side length for each number of elements tested in the mesh convergence case of a particle diameter of 100 μm and a domain height of 1,000 μm

Number of Elements (E)	N	Element Side Length (μm)
$1.4x10^4$	6	16.7
$4x10^4$	10	10
$3.6x10^5$	30	3.3
$6.4x10^5$	40	2.5
$1x10^6$	50	2
$9x10^6$	150	0.7

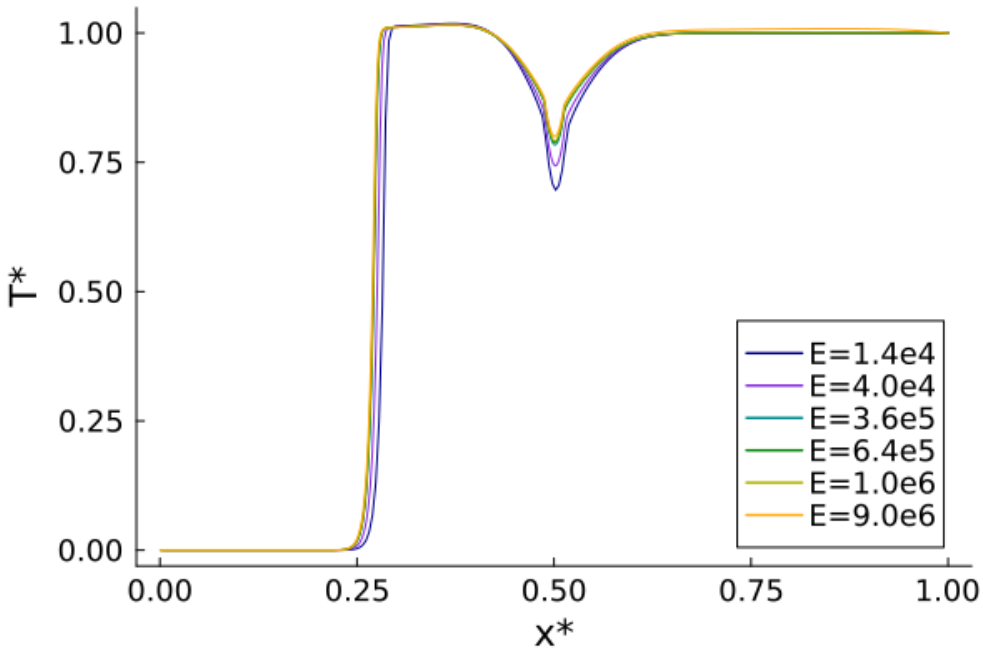

Figure 3.3: Center-line temperature profile at $y^* = L_y^*/2$ with varying mesh sizes. Corresponding element size and N value is presented in Table 3.2.

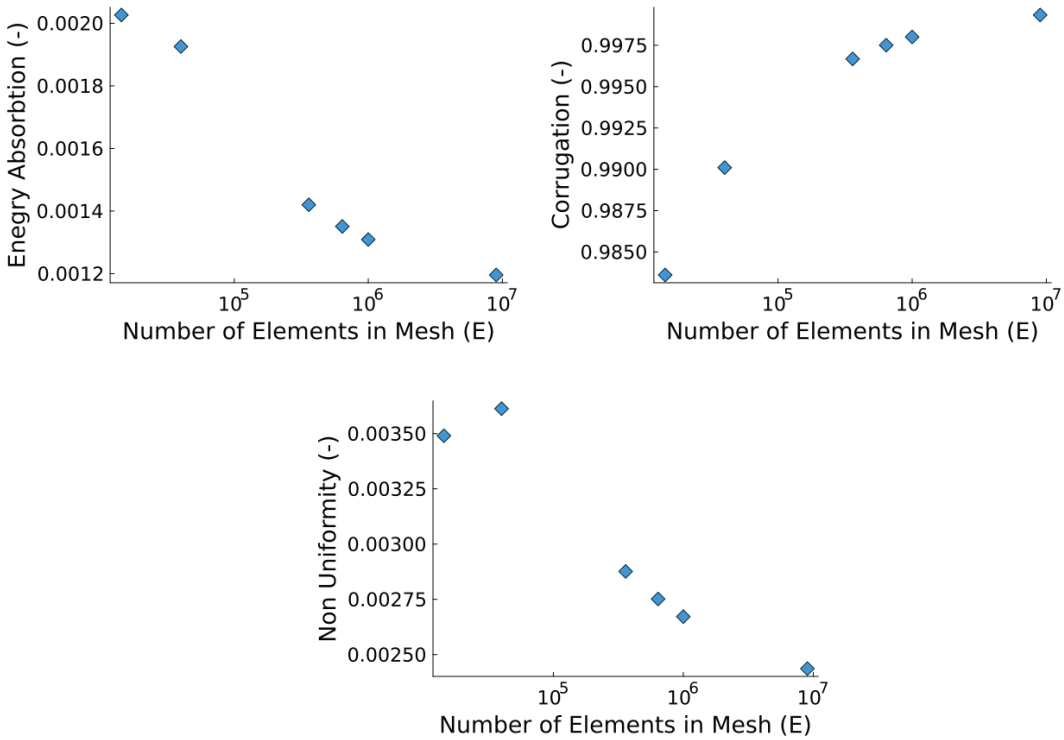

Figure 3.4: Calculated non-dimensional parameters with varying numbers of elements.

all simulations is equivalent to the diameter of the simulated particle divided by 50.

3.4 Determination of Domain Length

The application of the Neumann boundary at x^*=0 and L_x^* is synonymous with an insulating edge on the left and right ends of the simulation domain. The lack of conduction out of the domain in the direction of flame propagation can lead to an accumulation of heat at the edge of the simulation domain. The formation of this preheat zone accelerates the flame speed at the edge of the computational domain. To be sure that these edge effects brought on by the use of the Neumann boundary conditions do not impact the results of this study, a computational domain length of $L_x^* = 50$ was selected based on the fact the flame front was able to return to its steady state velocity before being accelerated by the end-effect preheat zone.

3.5 Flame Front Location and Evaluation Time

Energy absorption and temperature non-uniformity in a simulated particle were evaluated right after the flame front passed the particle. To determine when the flame front has passed the particle, the location of the flame front first needed to be described mathematically. This was accomplished by using linear interpolation to determine the location of a reaction

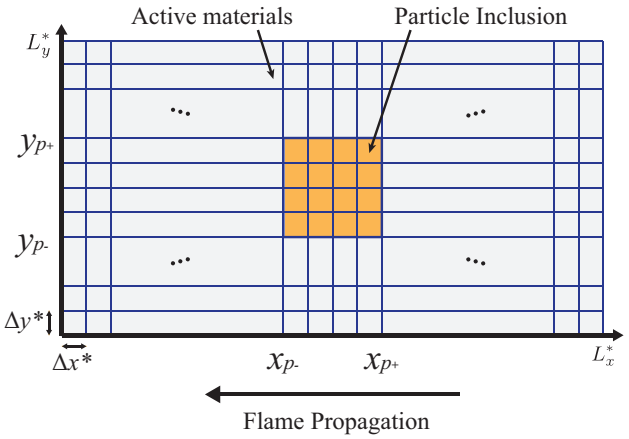

Figure 3.5: Schematic of the computational domain displaying the relevant coordinates used in Eq. 3.14 and direction of flame propagation.

completeness of 0.7. To implement this, the location of the flame front needs to be determined for every row y and every time t. To find the location of the flame front in the single row, y, we start be defining x_s, the subset of x values in this row where the reaction completeness is less than 0.7.

$$\mathbf{x_s} = \{x \in \mathbf{x} \mid \omega^*(x, y) < 0.7\} \tag{3.9}$$

After this subset is defined, the location of reaction completeness closest to 0.7 is given the variable name x_1.

$$(x_1, y) = ({}_{\mathbf{x_s}}[|\omega^*(\mathbf{x_s}, y) - 0.7|], y) \tag{3.10}$$

This is then repeated to determine the location of the value larger than 0.7.

$$\mathbf{x_g} = \{x \in \mathbf{x} \mid \omega^*(x, y) > 0.7\} \tag{3.11}$$

$$(x_2, y) = ({}_{\mathbf{x_g}}[|\omega^*(\mathbf{x_g}, y) - 0.7|], y_2) \tag{3.12}$$

Finally, these values are used in a linear interpolation to provide a prediction of the flame front location.

$$x = x_1 + \frac{x_2 - x_1}{\omega^*(x_2, y_2) - \omega^*(x_1, y_1)}(0.7 - \omega^*(x_1, y_1)) \tag{3.13}$$

This is repeated for every y value to attain a full flame front profile. The output of this algorithm is the location of the flame front $(\mathbf{x}, \mathbf{y})$ at every time step. The horizontal location of the flame front will now be described as a function of domain height and time, $x(t, y)$. The time at which the flame front passes the particle, t_a is described in Eq. 3.14. In this case, the flame propagation is from left to right. The flame front has passed the particle when all rows of the domain containing the particle ($y_{p_-} \leq y \leq y_{p_+}$, as shown in Fig. 3.5) are on the left side of the particle.

$$t_a = \min\{t \mid x(t, y_i) < x_{p_-} \quad \forall\ y_i \leq y_{p_+} \wedge y_i \geq y_{p_-}\} \tag{3.14}$$

$$t_a = \min\{t \mid x(t, y_{p_-} : y_{p_+}) < x_{p_-}\} \tag{3.15}$$

Sample results of the location of the flame front at this calculated time are included below in Fig. 3.6.

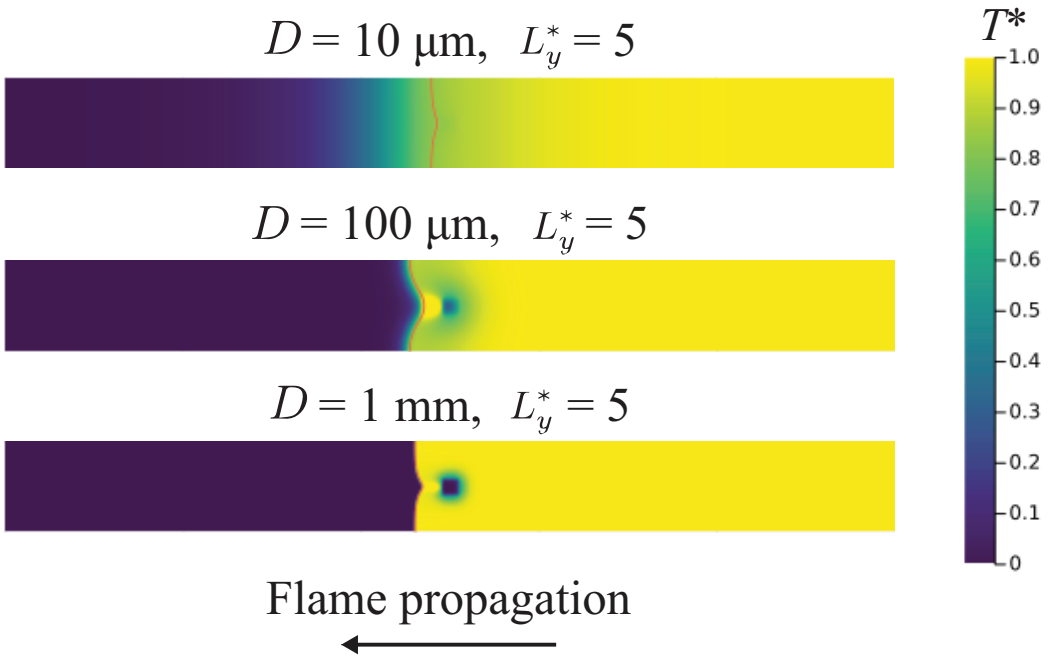

Figure 3.6: Dimensionless temperature fields ($T^*(x, y, t_a)$) at the selected inert particle diameter of D=10, 100, 1000 μm. A red curve in each temperature field denotes the location of the flame front.

Chapter 4

Results

4.1 Flame Propagation Measurements

Flame propagation tests were performed to understand the effects of SiO_2 particle sizes and mass loading on flame propagation. Figure 4.1a shows burning rates as a function of SiO_2 particle diameters at two different SiO_2 loadings of 2.5 wt% and 7.5 wt%. The baseline burning rate without SiO_2 additives was 4.32 cm/s. Similar to the previous studies observing contradiction to the laminar flame theory, particle inclusion of insulating SiO_2 in Al/CuO nanothermite films also showed improved burning rates with most particle sizes. At the SiO_2 mass loading of 7.5%, the particle size of 60-70 nm showed minimal change in burning rates. Note that 60-70 nm is the particle size closest to those of Al and CuO. However, as the SiO_2 particle size increases to 0.5-10 μm, the burning rate increases by 26.3%. Such burning rate increment is consistent with the result achieved by Kline et al. [18]. As we further increased the particle diameter, the burning rate decreased even slower than that of the baseline.

On the other hand, when the SiO_2 particle size is smaller than both Al and CuO, the burning rate dramatically increases by 145%. The nanoscale particle diameter results in a sintering time scale that is dramatically lower, likely to a value lower than that of the nanothermite, potentially changing the mechanism by which the particle and flame interact. This hypothesis is supported by the product analysis, showing irregularly aggregated product particles on the scale of 200 μm only with 10-20 nm SiO_2 additives (See the Section 5.1). Considering reactive sintering has previously been hypothesized to be the rate-liming step in

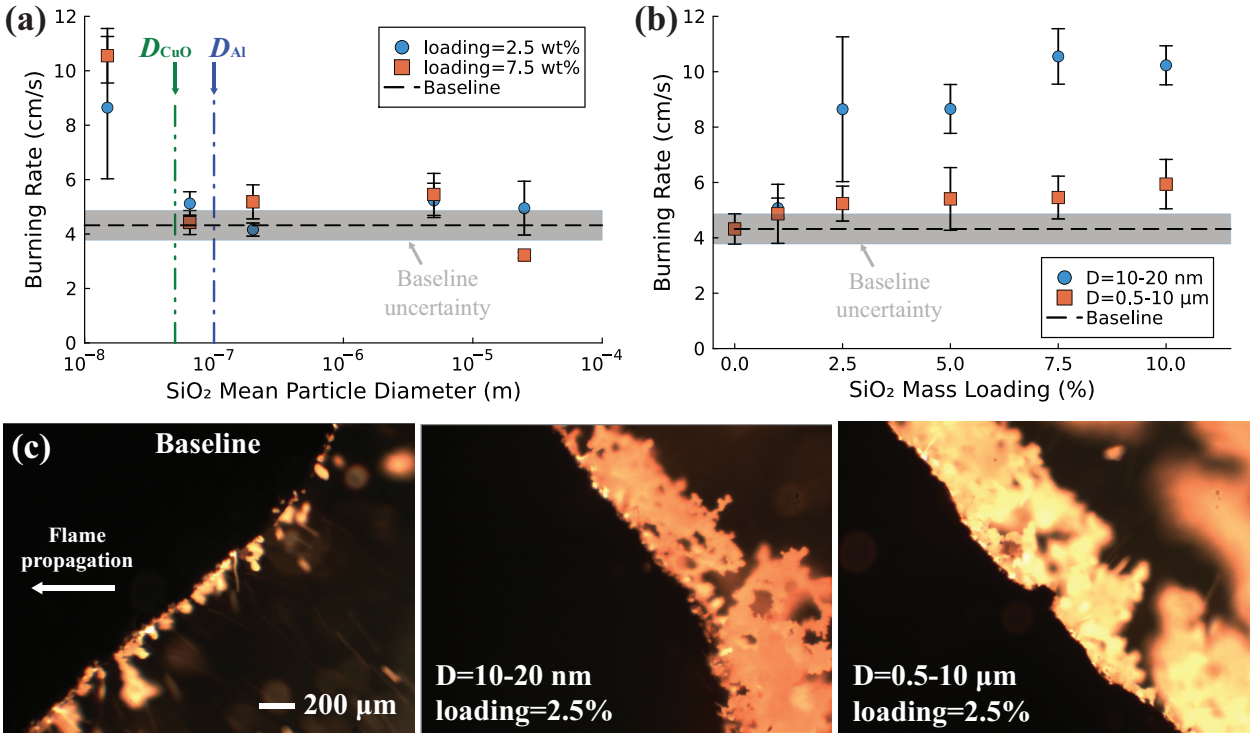

Figure 4.1: Experimental results obtained from the high-speed microscopic imaging system: (a) burning rates as a function of inert particle diameters in the logarithmic scale, (b) burning rates as a function of the SiO_2 mass loading, (c) still shots of flame morphologies for the baseline (left), D=10-20 nm SiO_2 (middle), and D=0.5-10 μm SiO_2 (right) at the SiO_2 mass loading of 2.5%. The scale bar applies to all still shots.

nanothermite combustion, this mechanism is likely to have a large impact on the observed macroscopic burning rate [27].

The previous study by Kline et al. [18] attributed such burning rate improvement to flame front corrugation. It is theorized that corrugation increases the flame front area, possibly accelerating the flame speed. To validate this hypothesis, the sub-millimeter-scale flame morphologies for the baseline and the inert particle inclusions of D_p=10-20 nm and 0.5-10 μm were shown in Fig. 4.1c. In all three cases, the significant difference in flame front corrugation is not visible. However, a thicker flame front was observed, suggesting that reaction products have a longer residence time on the film when SiO_2 is added. This creates a higher level of thermal feedback between the unreacted material and products, providing another possible explanation for the acceleration of the flame [15]. This change in flame front morphology may be due to the reduction in the adiabatic flame temperature caused by

the addition of SiO_2. This results in fewer vaporized products which can also be responsible for the ejection of solid and liquid products from the flame front. Yet, despite the similar flame front thickness, the burning rate of the 10-20 nm SiO_2 case is approximately two times faster than that of the 0.5-10 μm case, which implies another possible mechanism of burning rate alteration that requires further investigation.

From the experimental data, it is clear that particle size and weight percent both play an important role in the determination of the burning rate. Although previous work proposed a few mechanisms for burning rate control, they include multiple competing factors and cannot fully explain the trends observed experimentally. Such a gap motivated computational studies to achieve a deeper understanding of heat transfer processes between active energetic materials and inert particles.

4.2 Thermal Structures Modified by Additives

The simulation studies were carried out to understand the thermal behaviors around an inert particle when flame passes the particle. One-dimensional flame propagation was generated with the selected particle diameters and the domain heights as shown in Fig. 4.2a. Note that the domain size corresponds to the distance between two inert particles-which equivalently means the higher domain height, the smaller mass loading- as periodic boundary conditions were adopted for $y^* = 0$ and L_y^*.

Three selected cases show representative examples of how thermal structures can be changed by the inert particle and the domain height. Figure 4.2a shows the flame front distortion as a general trend while the flame front passes the particle in all three cases. In addition, these distortions are formed on a similar scale to the particle. However, the detailed thermal behaviors are dependent on the particle size and domain height.

In the case with D=100 μm and L_y^*=2, when the flame front is in contact with the particle, thermal thickness becomes significantly increased and the overall temperature decreases. As a result, the flame front slows down as shown in Fig. 4.2b, then propagates once the unreacted materials at the left side of the particle get heated over the ignition threshold. Indeed, since L_y^*=2 corresponds to a very high SiO_2 mass loading, the low energy density leads to slow

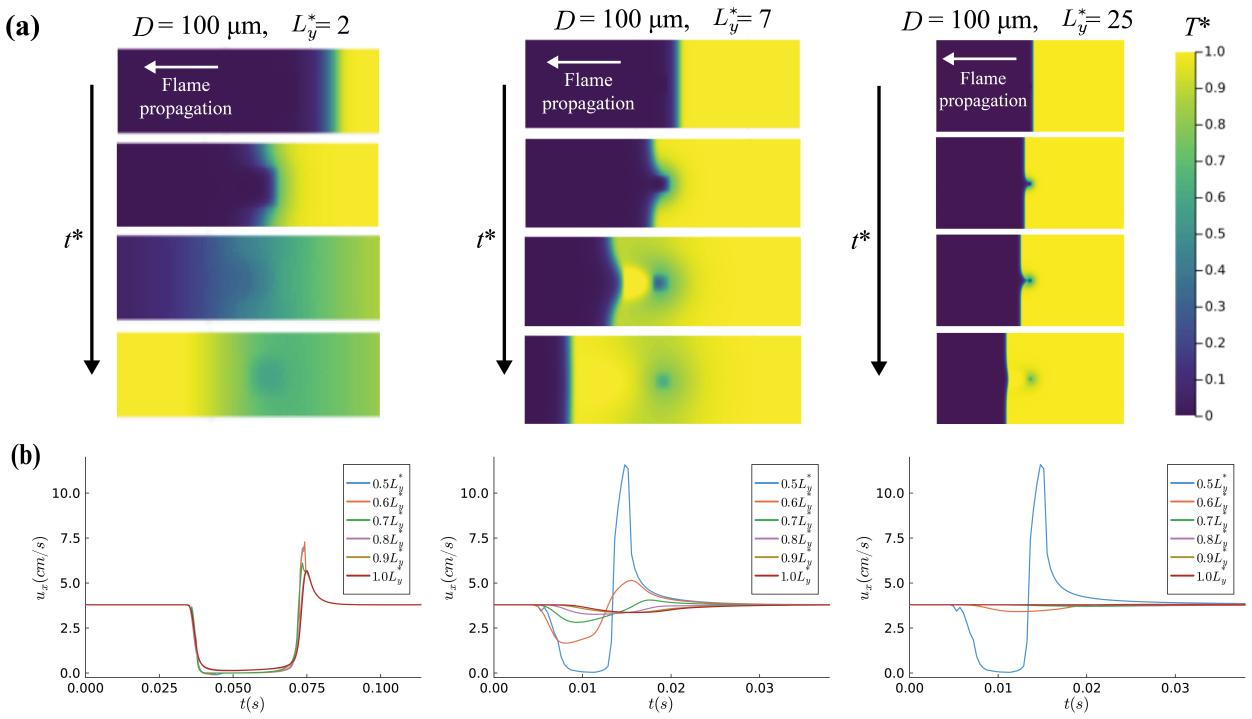

Figure 4.2: Simulation results: (a) Flame propagation and morphology for different particle sizes and domain heights. (b) Local propagation velocity at different y^* locations from center to top. D=100 μm and L_y^*=2 (left), D=100 μm and L_y^*=7 (middle), and D=1000 μm and L_y^*=10 (right).

flame propagation, resulting in enough time for the inert particle to remove heat from the surrounding energetic materials.

On the other hand, as the domain height L_y^* increases from 2 to 7, the available energy near an inert particle also increases. Unlike the case with L_y^*=2, the local flame distortion can be observed only close to the particle. Thus, the local flame front at the top boundary ($y^* = L_y^*$) propagates along the axial direction with a speed of the bulk burning rate (Fig. 4.2b). However, significant heat absorption is still visible in Fig. 4.2a while the flame front passes the particle. However, as we further increase the domain height L_y^* from 7 to 10 along with an increase in particle diameter from 100 μm to 1000 μm, these heat absorption in an inert particle can be merely found. The simulation results qualitatively show that flame corrugation could happen at the particle scale, but the amount of heat transfer between the inert particle and its surrounding energetic materials could significantly vary. Therefore, such corrugation, energy absorption, and temperature non-uniformity in an inert particle need to be systematically quantified to further understand how the particle inclusion changes the

flame front shape and removes heat from the energetic materials.

Chapter 5

Discussion

5.1 Sample Characterization

A large number of factors can contribute to changes in the burning rate. In some cases, the use of additives can result in greater porosity in the film, and a larger amount of "empty" space filled with air. Changes in porosity can alter heat transfer mechanisms in the film, as the amount of air dictates the thermal conductivity of the film and the extent to which convection is possible. To understand how the addition of SiO_2 affected the porosity of the films created, cross-sectional images of the Al/CuO/SiO_2 films cut with a razor were captured using an SEM. The images collected, shown in Fig. 5.1, displayed consistent thickness and porosity across different additive particle sizes and mass loadings. This suggests that changes in the observed burning rate are not due to differences in porosity between films.

The SEM was also used to image combustion products collected from a baseline case, 2.5 wt% 10-20 nm SiO_2, and 0.5-10 μ SiO_2. Collected images are displayed in Fig. 5.2. The product morphology of the baseline case and the 2.5 wt% 0.5-10 μm additive are very similar, they appear spherical with a distribution of diameters of about 30 μm and smaller. The 2.5 wt% 10-20 nm μm additive products, however, display a very different morphology. There were large aggregates of particles that were several hundred microns large.

This product analysis suggests that the addition of 10-20 nm SiO_2 resulted in changes to the particle sintering occurring during the reaction. This provides a possible explanation for the significantly higher burn rate compared to other additive sizes. These results also

necessitate future work as the focus of this study is on thermal interaction, and as such modeling efforts do not include sintering and therefore are not able to capture the physics of this large burning rate increase.

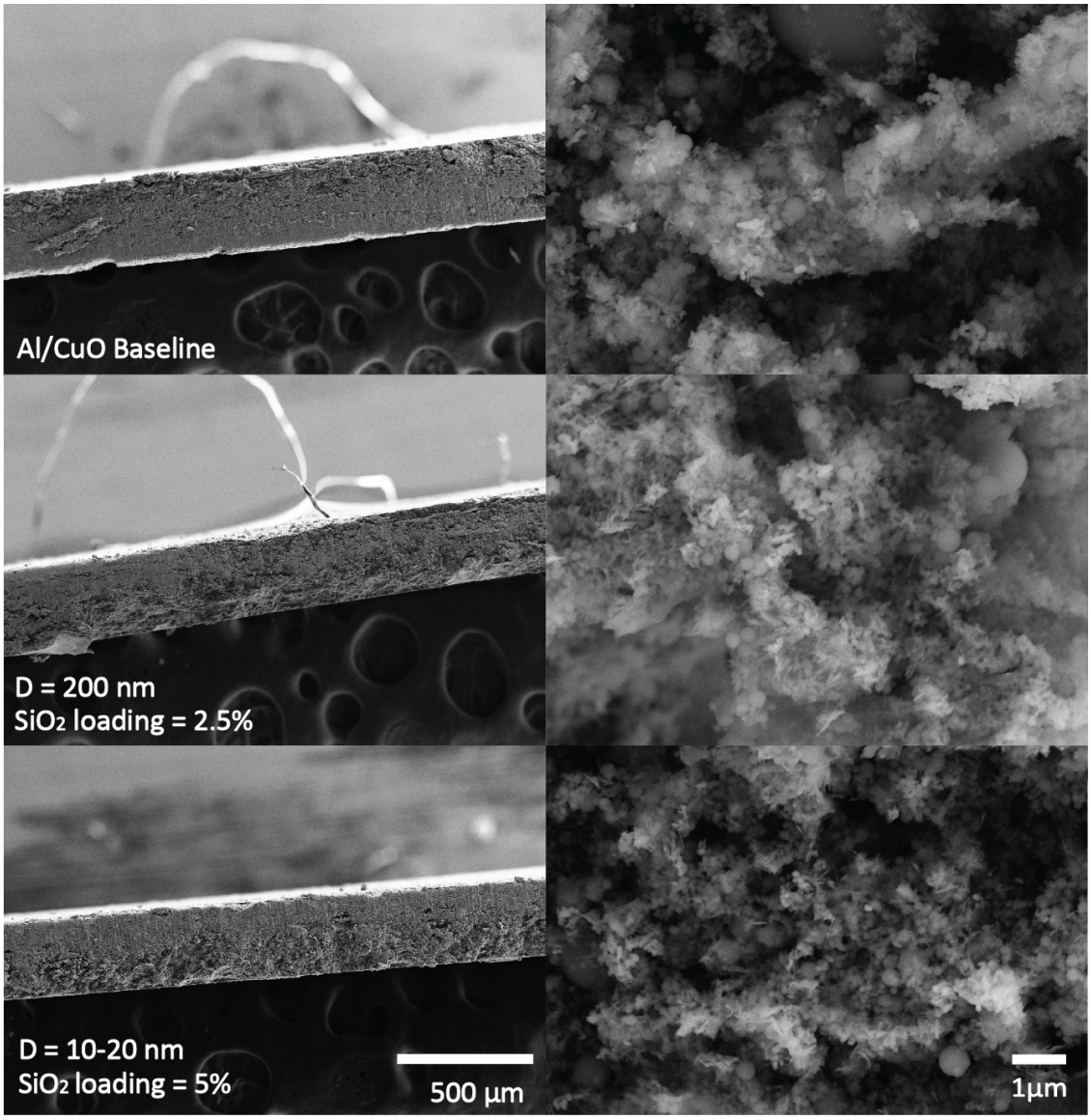

Figure 5.1: Cross-sectional images of three films with varying SiO_2 mass loading and particle sizes. Films were cut using a razor blade to obtain cross-section and they do not display visible differences in porosity.

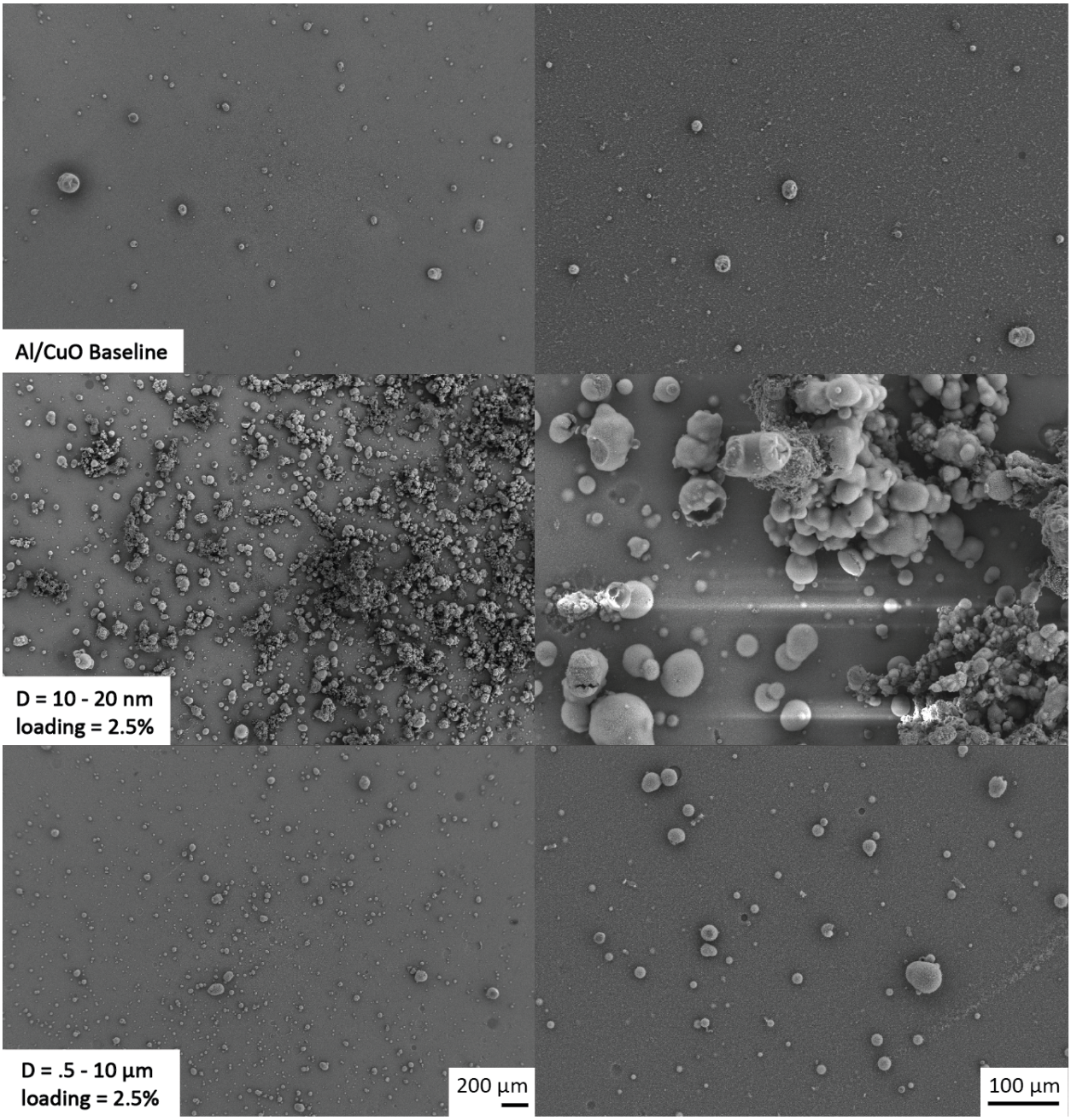

Figure 5.2: SEM images of combustion products from 2.5 weight percent SiO_2 films with varied particle size. A baseline 0 percent SiO_2 case is also included. Differences between the 10-20 nm and the baseline case are significantly more dramatic than for the .5-10 nm additive case.

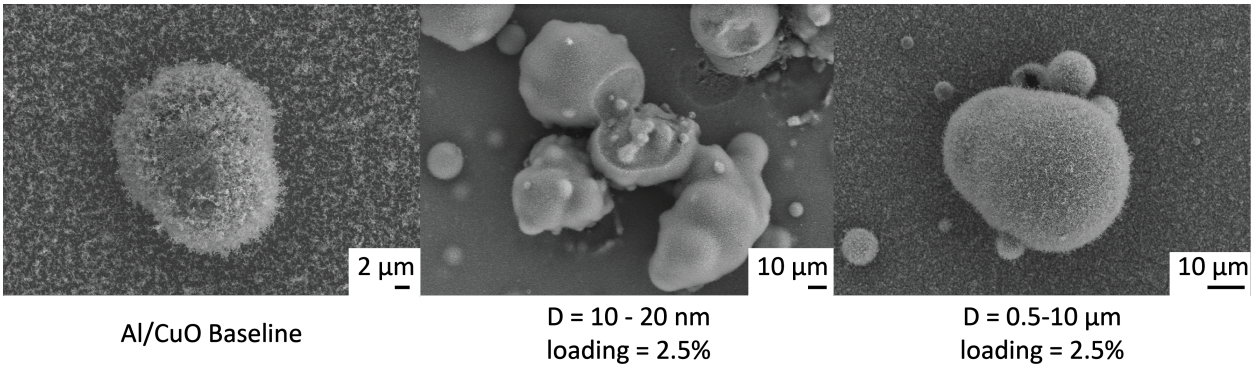

Figure 5.3: SEM images of combustion products from 2.5 weight percent SiO_2 films with varied particle size. A baseline 0 percent SiO_2 case is also included. Differences between the 10-20 nm and the baseline case are significantly more dramatic than for the .5-10 nm additive case.

5.2 Non-dimensional Analysis of Thermal Interaction

The simulation results showed that temperature in the inert particle and flame morphology are strongly dependent on the particle size and the domain height. To systematically understand these effects and to relate these simulation results to the experimental observations, non-dimensional parameter analyses were employed with mass loading ($m_{\text{inert}}/m_{\text{total}}$) and Fourier number (Fo$=\alpha t/D^2 = \alpha/r_b D$). The Fourier number was chosen to characterize the ratio between the time the flame front passes through the particle and the time for the inert particle to heat up. Note that r_b was fixed as the baseline burning rate, obtained by experiments, for all the analyses.

Since excessive inert particle additives will eventually decrease the energy density of the nanothermite composite and hence the burning rate, we aim to comprehend the observation in Fig. 4.1 that certain mass loading actually increases the burning rate. According to Kline et al. [18], the flame corrugation induced by inert particles is responsible for the burning rate enhancement. Therefore, the flame front corrugation will be characterized. Moreover, the influence of temperature gradient hypothesized by Julien et at. [19] will be characterized by the temperature non-uniformity metrics. Finally, we further define a metric for the effect of inert particles as a heat sink.

The three dimensionless metrics are as follows: flame front corrugation (FC, Eq. (5.1)),

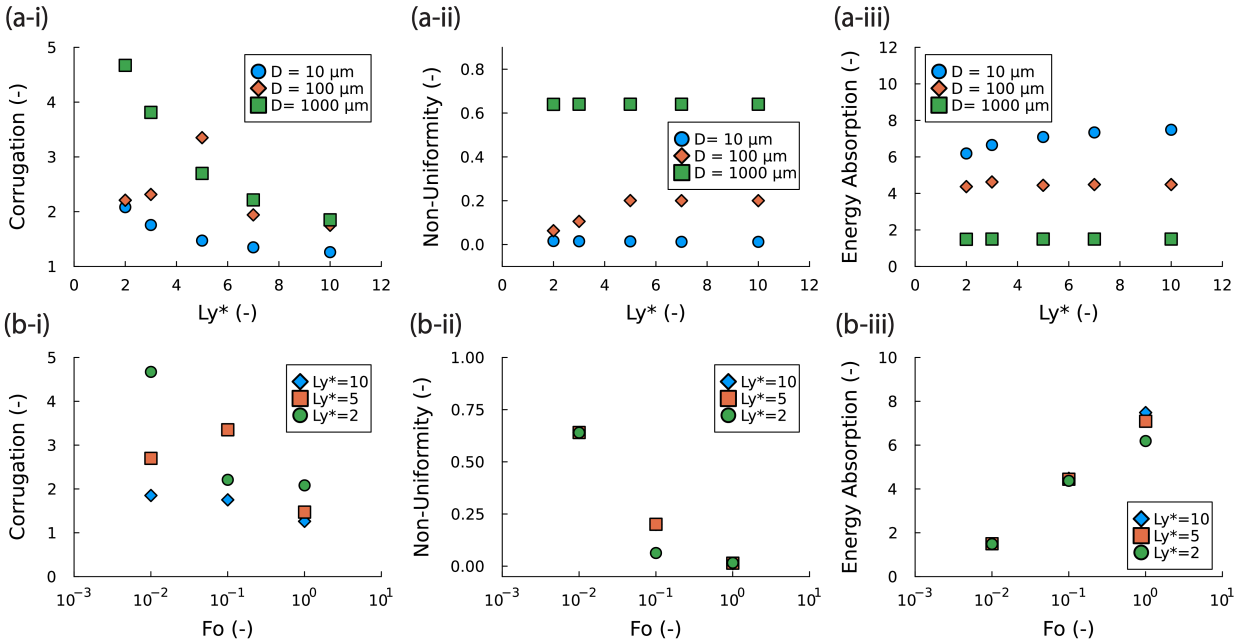

Figure 5.4: Quantification of heat transfer between the inert particle and surrounding active energetic materials and flame corrugation as a function of (a) domain height (L_y^*) and (b) Fourier number (Fo). Key metrics: (i) flame front corrugation, (ii) temperature non-uniformity, and (iii) energy absorption. For reference, D=10, 100, 1000 μm correspond to Fo=1, 0.1, 0.01, respectively.

temperature non-uniformity arising in a particle (TN, Eq. (5.2)), and particle energy absorption (EA, Eq. (5.3)), to quantify the heat transfer and the flame morphology.

$$\mathrm{FC} = \frac{L_{\mathrm{flame}}}{L_{\mathrm{domain\ height}}}, \tag{5.1}$$

$$\mathrm{TN} = \frac{1}{T_m}\left[\frac{1}{N}\sum_{x,y}^{N}(T(x,y) - T_m)^2\right]^{\frac{1}{2}}, \tag{5.2}$$

$$\mathrm{EA} = \frac{E - E_0}{E_0} = \frac{T_m - T_0}{T_0}, \tag{5.3}$$

where L is the length, T is temperature, subscript 0 and m demote the reference state and the mean value, respectively, and E is the internal energy. Eqs. 5.1-5.3 are computed between two states: the initial condition and directly after the flame front passes the particle, as described in Section 3.5.

To understand the effects of the inert particle mass loading on flame corrugation, temperature non-uniformity, and energy absorption, simulations were performed by varying domain

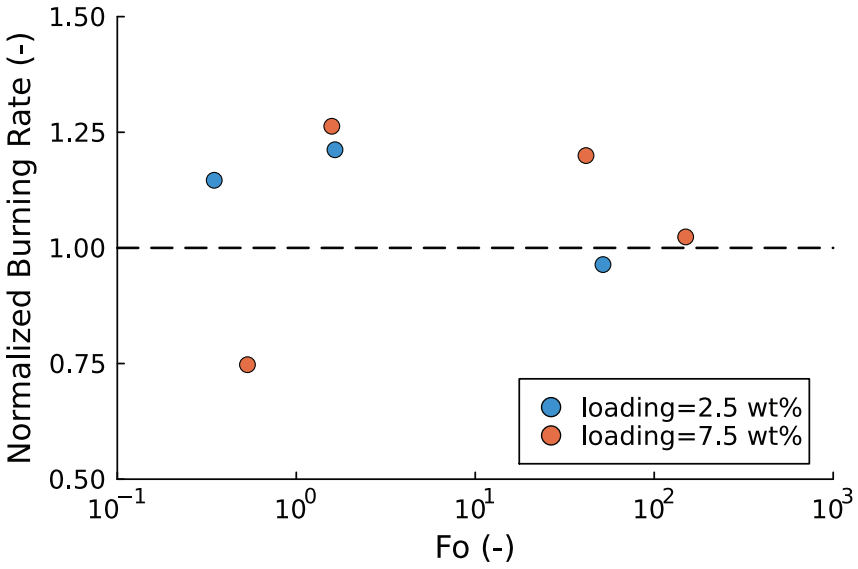

Figure 5.5: Correlations between the normalized burning rate and the Fourier number. The experimentally obtained burning rates with particle inclusion were normalized by the baseline burning rate without particle inclusion.

heights for fixed inert particle sizes. Figure 5.4a shows three metrics as a function of domain height. Note that periodic boundary conditions were specified in the y-direction, so the larger the domain height, the smaller the particle loading. There is no clear trend in the flame corrugation metric as the domain height changes. Specifically, while flame corrugation decreases with the largest and smallest particle sizes, flame corrugation shows a nonmonotonic behavior for the middle-sized case. However, such influence only applies to relatively small domain height, corresponding to relatively high inert particle loading (>25 wt%). The flame corrugation effect shows a decreasing trend as the loading further decreases. On the other hand, both the energy absorption and the temperature non-uniformity metrics have a weak positive correlation with domain height with particles of all sizes. Surprisingly, the more the mass loading, the less the energy absorption in the inert particle (or the energy loss in the active energetic materials).

We further investigate the effects of the Fourier number (heat transfer inside the inert particle) on these metrics. Note that the larger the particle diameter, the smaller the Fourier number, given the fixed burning rate. Figure 5.4b shows flame corrugation can be observed in all cases at a similar level. However, strong correlations between the temperature non-uniformity and energy absorption to Fourier number are shown. As the Fourier number

increases, the temperature non-uniformity decreases while the energy absorption increases. Recalling that the Fourier number characterizes the residence time of the particle in the flame front compared to the time needed to heat up the inert particle, the correlations suggest that the inert particles act as insulators when Fo is small. Recalling again that Fo decreases as particle size increases, this suggests that a larger particle absorbs less heat and may experience larger temperature gradients from the particle surface to the center. In other words, a large particle is not fully heated while the flame passes the particle. Therefore, this particle results in flame corrugation with minimal penalties of drawing heat away from the active energetic materials. In summary, while flame corrugation is widely observed by adding inert particles to active energetic materials, the intricate heat transfer process in the inert particles needs to be considered to explain the trend observed in different inert particle sizes and mass loading cases.

We finally compare these findings with the experimental results. Generally, the burning rates increase with the particle size and mass loading in Fig. 4.1 (non-dimensional version in Fig. 5.5) when inert particle sizes do not significantly deviate from the Al and CuO sizes. With a large particle size, heat loss in active energetic materials can be reduced while it shows a transient heating process with temperature non-uniformity, leading to an increase in the burning rates in the experiments. Flame front corrugation plausibly increases the reaction front area, also resulting in a burning rate increase. However, since such corrugation is also affected by the energy absorption in inert particles, both thermal interaction between inert particles and energetic materials and flame front corrugation should be taken into account to properly tune the burning rates with additives.

Chapter 6

Conclusion and Future Work

6.1 Conclusion

In this study, we systematically investigated how heat transfer between inert particles and their surrounding energetic materials modifies the burning rates. The experimental results with a microscopic high-speed imaging system have shown that the burning rates increase with an increase in particle diameter in the range of 100 nm and 100 μm and SiO_2 mass loading in all measured ranges. At a particle diameter smaller than both Al and CuO, a drastic increase in burning rate was observed presumably due to fast reactive sintering processes, which is still an open question and out of the scope of the current study.

Further simulation studies have revealed that the heat loss in energetic materials surrounding inert particles may vary with particle sizes and mass loading. These heat transfer effects were quantified in two metrics of energy absorption and temperature non-uniformity in an inert particle, along with the flame front corrugation. The non-dimensional analyses have shown that flame corrugation is observed for all particle sizes and mass loading, which concludes that flame corrugation may not be the sole factor to alter the burning rate. On the other hand, energy absorption and temperature non-uniformity in an inert particle have strong correlations with particle diameter while they have weak correlations with the mass loading. When the residence time of the inert particle inside the flame front is relatively long compared to the time to heat it up, it acts as a heat sink. As a result, while inert particles cause flame corrugation, at the same mass loading, smaller particles further remove

heat from active energetic materials. Such non-dimensional analysis explained the measured burning rate variations with controlled inert particle sizes and mass loading. The findings can provide guidelines for the development of energetic materials with tunable performance.

6.2 Future Work

The addition of 10-20 nm SiO_2, smaller than both the Al and CuO, resulted in a burn rate increase of 145%. The measured burn rates were significantly higher with this super fine additive than with any of the larger particle sizes. To understand this phenomenon combustion products were collected from three different films and imaged using an SEM. These images revealed that products from films with the super fine additive had a different morphology compared to the baseline case and films with larger additive particles. To fully understand the physics responsible for this change in burning rate, a mechanism study should be conducted to characterize the chemical reactions and thermal properties of micron and nano-sized SiO_2 additives. Future work will likely necessitate the use of more advanced diagnostics. Analysis of product composition and in-situ temperature measurements (such as pyrometry) could both provide additional insights into how reaction chemistry may be altered by these additives. Additionally, a more complete understanding of chemical interaction such as catalytic effects between SiO_2 and the Al/CuO film, including binder materials, would be advantageous. Finally, this study should be repeated with additives other than SiO_2. The current theory is that these trends in burning rate are due to the silicon dioxide's insulating properties, but this needs to be verified using other insulting additives.

References

[1] R. A. Yetter, "Progress towards nanoengineered energetic materials," *Proceedings of the Combustion Institute*, vol. 38, no. 1, pp. 57–81, Jan. 2021, ISSN: 1540-7489. DOI: 10.1016/j.proci.2020.09.008.

[2] N.-S. Jang, S.-H. Ha, K.-H. Kim, M. H. Cho, S. H. Kim, and J.-M. Kim, "Low-power focused-laser-assisted remote ignition of nanoenergetic materials and application to a disposable membrane actuator," *Combustion and Flame*, vol. 182, pp. 58–63, Aug. 2017, ISSN: 0010-2180. DOI: 10.1016/j.combustflame.2017.04.021.

[3] K.-i. Koo, M.-J. Jeong, S. Park, H. Choi, G.-s. Kim, and D. ". Cho, "Novel Valveless Micro Suction Pump Using a Solid Chemical Propellant," in *World Congress on Medical Physics and Biomedical Engineering 2006*, R. Magjarevic and J. H. Nagel, Eds., Berlin, Heidelberg: Springer, 2007, pp. 310–313, ISBN: 978-3-540-36841-0. DOI: 10.1007/978-3-540-36841-0_86.

[4] M. Wehner, R. L. Truby, D. J. Fitzgerald, B. Mosadegh, G. M. Whitesides, J. A. Lewis, and R. J. Wood, "An integrated design and fabrication strategy for entirely soft, autonomous robots," en, *Nature*, vol. 536, no. 7617, pp. 451–455, Aug. 2016, Number: 7617 Publisher: Nature Publishing Group, ISSN: 1476-4687. DOI: 10.1038/nature19100.

[5] S. D. Heister, W. E. Anderson, T. L. Pourpoint, and R. J. Cassady, *Rocket Propulsion*, en, ISBN: 9781108381376 Publisher: Cambridge University Press, Feb. 2019. DOI: 10.1017/9781108381376.

[6] R. S. Janesheski, L. J. Groven, and S. Son, "Fluoropolymer and aluminum piezoelectric reactives," *AIP Conference Proceedings*, vol. 1426, no. 1, pp. 741–744, Mar. 2012, ISSN: 0094-243X. DOI: 10.1063/1.3686385.

[7] J. H. (Shin and M. Zhou, "Piezoelectric response of energetic composites under an electrostatic excitation," en, *Journal of Applied Physics*, vol. 129, no. 24, p. 245 103, Jun. 2021, ISSN: 0021-8979, 1089-7550. DOI: 10.1063/5.0049124.

[8] L. Bao, H. Wang, Z. Wang, H. Xie, S. Xiang, X. Zhang, W. Zhang, Y. Huang, R. Shen, and Y. Ye, "Controllable ignition, combustion and extinguishment characteristics of HAN-based solid propellant stimulated by electric energy," *Combustion and Flame*, vol. 236, p. 111 804, Feb. 2022, ISSN: 0010-2180. DOI: 10.1016/j.combustflame.2021.111804.

[9] S. J. Barkley, K. Zhu, J. E. Lynch, J. B. Michael, and T. R. Sippel, "Microwave plasma enhancement of multiphase flames: On-demand control of solid propellant burning rate," *Combustion and Flame*, vol. 199, pp. 14–23, Jan. 2019, ISSN: 0010-2180. DOI: 10.1016/j.combustflame.2018.10.007.

[10] S. Isakari, T. Asakura, D. Haraguchi, Y. Yano, and A. Kakami, "Performance evaluation and thermography of solid-propellant microthrusters with laser-based throttling," *Aerospace Science and Technology*, vol. 71, pp. 99–108, Dec. 2017, ISSN: 1270-9638. DOI: 10.1016/j.ast.2017.08.027.

[11] R. A. Chandru, N. Balasubramanian, C. Oommen, and B. N. Raghunandan, "Additive Manufacturing of Solid Rocket Propellant Grains," *Journal of Propulsion and Power*, vol. 34, no. 4, pp. 1090–1093, 2018, Publisher: American Institute of Aeronautics and Astronautics _eprint: https://doi.org/10.2514/1.B36734, ISSN: 0748-4658. DOI: 10.2514/1.B36734.

[12] I. E. Gunduz, M. S. McClain, P. Cattani, G. T. .-. Chiu, J. F. Rhoads, and S. F. Son, "3D printing of extremely viscous materials using ultrasonic vibrations," *Additive Manufacturing*, vol. 22, pp. 98–103, Aug. 2018, ISSN: 2214-8604. DOI: 10.1016/j.addma.2018.04.029.

[13] M. S. McClain, I. E. Gunduz, and S. F. Son, "Additive manufacturing of ammonium perchlorate composite propellant with high solids loadings," *Proceedings of the Combustion Institute*, vol. 37, no. 3, pp. 3135–3142, Jan. 2019, ISSN: 1540-7489. DOI: 10.1016/j.proci.2018.05.052.

[14] Q.-L. Yan, F.-Q. Zhao, K. K. Kuo, X.-H. Zhang, S. Zeman, and L. T. DeLuca, "Catalytic effects of nano additives on decomposition and combustion of RDX-, HMX-, and AP-based energetic compositions," *Progress in Energy and Combustion Science*, vol. 57, pp. 75–136, Nov. 2016, ISSN: 0360-1285. DOI: 10.1016/j.pecs.2016.08.002.

[15] H. Wang, D. J. Kline, M. C. Rehwoldt, and M. R. Zachariah, "Carbon Fibers Enhance the Propagation of High Loading Nanothermites: In Situ Observation of Microscopic Combustion," *ACS Applied Materials & Interfaces*, vol. 13, no. 26, pp. 30 504–30 511, Jul. 2021, Publisher: American Chemical Society, ISSN: 1944-8244. DOI: 10.1021/acsami.1c02911.

[16] C. Huang, G. Jian, J. B. DeLisio, H. Wang, and M. R. Zachariah, "Electrospray Deposition of Energetic Polymer Nanocomposites with High Mass Particle Loadings: A Prelude to 3D Printing of Rocket Motors," en, *Advanced Engineering Materials*, vol. 17, no. 1, pp. 95–101, 2015, _eprint: https://onlinelibrary.wiley.com/doi/pdf/10.1002/adem.201400151, ISSN: 1527-2648. DOI: 10.1002/adem.201400151.

[17] H. Wang, J. B. DeLisio, S. Holdren, T. Wu, Y. Yang, J. Hu, and M. R. Zachariah, "Mesoporous Silica Spheres Incorporated Aluminum/Poly (Vinylidene Fluoride) for Enhanced Burning Propellants," en, *Advanced Engineering Materials*, vol. 20, no. 2, p. 1 700 547, 2018, _eprint: https://onlinelibrary.wiley.com/doi/pdf/10.1002/adem.201700547, ISSN: 1527-2648. DOI: 10.1002/adem.201700547.

[18] D. J. Kline, M. C. Rehwoldt, H. Wang, N. E. Eckman, and M. R. Zachariah, "Why does adding a poor thermal conductor increase propagation rate in solid propellants?" *Applied Physics Letters*, vol. 115, no. 11, p. 114 101, Sep. 2019, ISSN: 0003-6951. DOI: 10.1063/1.5113612.

[19] B. Julien, H. Wang, E. Tichtchenko, S. Pelloquin, A. Esteve, M. R. Zachariah, and C. Rossi, "Elucidating the dominant mechanisms in burn rate increase of thermite nanolaminates incorporating nanoparticle inclusions," en, *Nanotechnology*, vol. 32, no. 21, p. 215 401, Mar. 2021, Publisher: IOP Publishing, ISSN: 0957-4484. DOI: 10.1088/1361-6528/abe6c8.

[20] G. V. Ivanov and F. Tepper, "'ACTIVATED' ALUMINUM AS A STORED ENERGY SOURCE FOR PROPELLANTS," English, *International Journal of Energetic Materials and Chemical Propulsion*, vol. 4, no. 1-6, 1997, Publisher: Begel House Inc., ISSN: 2150-766X, 2150-7678. DOI: 10.1615/IntJEnergeticMaterialsChemProp.v4.i1-6.600.

[21] L. T. De Luca, L. Galfetti, F. Severini, L. Meda, G. Marra, A. B. Vorozhtsov, V. S. Sedoi, and V. A. Babuk, "Burning of Nano-Aluminized Composite Rocket Propellants," en, *Combustion, Explosion and Shock Waves*, vol. 41, no. 6, pp. 680–692, Nov. 2005, ISSN: 1573-8345. DOI: 10.1007/s10573-005-0080-5.

[22] I. Glassman, R. A. Yetter, and N. G. Glumac, *Combustion*, en. Academic Press, Dec. 2014, Google-Books-ID: lLJZAwAAQBAJ, ISBN: 978-0-12-411555-2.

[23] Y. Huang, G. A. Risha, V. Yang, and R. A. Yetter, "Combustion of bimodal nano/micron-sized aluminum particle dust in air," *Proceedings of the Combustion Institute*, vol. 31, no. 2, pp. 2001–2009, Jan. 2007, ISSN: 1540-7489. DOI: 10.1016/j.proci.2006.08.103.

[24] P. Lynch, G. Fiore, H. Krier, and N. Glumac, "Gas-Phase Reaction in Nanoaluminum Combustion," *Combustion Science and Technology*, vol. 182, no. 7, pp. 842–857, Jun. 2010, Publisher: Taylor & Francis _eprint: https://doi.org/10.1080/00102200903341561, ISSN: 0010-2202. DOI: 10.1080/00102200903341561.

[25] K. T. Sullivan, N. W. Piekiel, C. Wu, S. Chowdhury, S. T. Kelly, T. C. Hufnagel, K. Fezzaa, and M. R. Zachariah, "Reactive sintering: An important component in the combustion of nanocomposite thermites," *Combustion and Flame*, vol. 159, no. 1, pp. 2–15, Jan. 2012, ISSN: 0010-2180. DOI: 10.1016/j.combustflame.2011.07.015.

[26] P. Chakraborty and M. R. Zachariah, "Do nanoenergetic particles remain nano-sized during combustion?" *Combustion and Flame*, vol. 161, no. 5, pp. 1408–1416, May 2014, ISSN: 0010-2180. DOI: 10.1016/j.combustflame.2013.10.017.

[27] H. Wang, D. J. Kline, and M. R. Zachariah, "In-operando high-speed microscopy and thermometry of reaction propagation and sintering in a nanocomposite," en, *Nature Communications*, vol. 10, no. 1, p. 3032, Jul. 2019, Number: 1 Publisher: Nature Publishing Group, ISSN: 2041-1723. DOI: 10.1038/s41467-019-10843-4.

[28] J. Wang, A. Hu, J. Persic, J. Z. Wen, and Y. Norman Zhou, "Thermal stability and reaction properties of passivated Al/CuO nano-thermite," *Journal of Physics and Chemistry of Solids*, vol. 72, no. 6, pp. 620–625, Jun. 2011, ISSN: 0022-3697. DOI: 10.1016/j.jpcs.2011.02.006.

[29] L. Zhou, N. Piekiel, S. Chowdhury, and M. R. Zachariah, "T-Jump/time-of-flight mass spectrometry for time-resolved analysis of energetic materials," en, *Rapid Communications in Mass Spectrometry*, vol. 23, no. 1, pp. 194–202, 2009, _eprint: https://onlinelibrary.wiley.com/ ISSN: 1097-0231. DOI: 10.1002/rcm.3815.

[30] S. Kim, A. A. Johns, J. Z. Wen, and S. Deng, "Burning structures and propagation mechanisms of nanothermites," *Proceedings of the Combustion Institute*, vol. 39, no. 3, pp. 3593–3604, Jan. 2023, ISSN: 1540-7489. DOI: 10.1016/j.proci.2022.07.113.

[31] J. M. Epps, J.-P. Hickey, and J. Z. Wen, "Modelling reaction propagation for Al/CuO nanothermite pellet combustion," *Combustion and Flame*, vol. 229, p. 111 374, Jul. 2021, ISSN: 0010-2180. DOI: 10.1016/j.combustflame.2021.02.020.

[32] P. J. Linstrom and W. G. Mallard, "The NIST Chemistry WebBook: A chemical data resource on the internet," *J. Chem. Eng. Data*, vol. 46, no. 5, pp. 1059–1063, 2001.

[33] S. Fischer and M. Grubelich, "A survey of combustible metals thermites and intermetallics for pyrotechnic applications," p. 15, Jul. 1996.

[34] S. M. Umbrajkar, M. Schoenitz, and E. L. Dreizin, "Exothermic reactions in Al–CuO nanocomposites," *Thermochimica Acta*, vol. 451, no. 1, pp. 34–43, Dec. 2006, ISSN: 0040-6031. DOI: 10.1016/j.tca.2006.09.002.

[35] M. C. Rehwoldt, D. J. Kline, and M. R. Zachariah, "Numerically evaluating energetic composite flame propagation with thermally conductive, high aspect ratio fillers," *Chemical Engineering Science*, vol. 229, p. 116 087, Jan. 2021, ISSN: 0009-2509. DOI: 10.1016/j.ces.2020.116087.